Phase Transformations in an AISI 410S Stainless Steel Observed in Directional and Laser-induced Cooling Regimes

Milton Sergio Fernandes de Lima[a]*, Ana Maria do Espirito Santo*[b]

[a]*Instituto de Estudos Avançados – IEAv, Centro Técnico Aeroespacial – CTA,
CEP 12228-970, São José dos Campos, SP, Brazil*
[b]*Departamento de Ciências Exatas e da Terra, Instituto de Ciências Ambientais,
Químicas e Farmacêuticas, Universidade Federal de São Paulo – UNIFESP,
Campus Diadema, CEP 09972-270, Diadema, SP, Brazil*

The applications of the chromium ferritic stainless steel AISI 410S have been considerably increased in the last years in many technical fields as chemical industries and oil or gas transportation. However, the phase transformation temperatures are, currently, unknown for this alloy. The aim of this work is to determine the alpha to gamma transformation temperatures of the AISI 410S alloy in different cooling conditions and to analyze them using continuous cooling theory. In order to achieve different cooling rates and thermal conditions, two complementary techniques were used: Bridgman furnace crystal growth and laser remelting technique. The measured solidification temperature was around 1730 and 1750 K. Plate-like and dendritic austenite precipitates were obtained in solid-state phase using growth rates between 5 and 10 µm/s in directional growth experiments. Only plate-like austenite phase was observed in the experiments using growth rates above 100 µm/s. The appearance of dendrites, with the consequent segregation of the elements, can be previously determined by the microstructure modeling currently proposed. Massive austenite can be produced from 0.3 to 10 mm/s rates at temperatures between 1100-1300 K. The structure might be less sensitive to corrosion because this phase is produced without microsegregation.

Keywords: *continuous cooling theory, directional solidification, Bridgman, laser remelting*

1. Introduction

The applications of chromium ferritic stainless steels have been considerably increased in the last years in many technical fields as chemical industries and oil or gas transportation. Thanks to the combination of its high-corrosion resistance and good mechanical properties[1], these alloys can be found in different environments as cargo ships and external architectural facades. Currently, the industries reduce the use of strategic and costly metals, such as Ni, and prefer metals which maintain the corrosion and mechanical properties near to that of austenitic grade stainless steels. For this, the AISI 410S (European grade 1.4003) with 10.5-12.5% Cr and less than 1% Ni was developed[2,3].

Although, the final microstructure is known to be composed by variable amounts of ferrite and martensite, still the 410S duplex microstructure is not well understood. Especially, the effect of cooling rate on the formation of the austenite phase and the microsegregation pattern linked to the ferrite-austenite transformation are even unclear[4]. It is known that AISI new requirements of the petroleum refining industry[5-8] need further research about the microstructure evolution during solidification and solid-state transformations of these steels.

Most of the phase transformation studies in ferritic/austenitic steels[9-111], were based on isothermal treatments.

This method usually requires a large number of specimens for a complete description of reactions. On the other hand, crystal growth techniques like Bridgman[12] can offer a very controlled way to verify the influence of processing conditions on the kinetics of phase transformations in a single sample. In this case, the growth is imposed by the continuous displacement of isotherms (isovelocity) when the sample is displaced on the vertical axis from the equipment furnace to a quenching medium. Thus, the transformation interface is constrained to assume a given growth morphology and temperature. Phase growth studies using directional solidification have been carried out by a number of authors, like Trivedi et al. for the Al-Cu system[13], Lima and Kurz[14] for the Fe-Cr and Fe-Ni systems and Jacot et al.[15] for Fe-Co alloys.

Although very useful, the Bridgman method has some limitations on growth rate. In order to obtain higher growth rates than those of Bridgman, laser conduction welding can be very helpful. Laser beam scans the material surface in order to melt a small volume of it. As the metal is a good heat sink, the melted layer is resolidified just behind the melt pool, and finally, solid-state phase transformations could occur. The method produces continuous cooling at the weld centerline at speeds related to the laser beam displacement. The weld zone is tiny compared to the Bridgman case and

*e-mail: msflima@gmail.com

the thermal gradient is consequently higher. Laser beam welding has been used to study phase transformation in a number of systems such as Al-Si[16], Al-Cu[17], Fe-C[18] and some multicomponent materials[19,20].

The aim of this work is to determine the alpha to gamma transformation temperatures of the AISI 410S alloy for different cooling conditions and compare them with those obtained from the continuous cooling theory.

2. Modeling Phase Transformations

The growth theory used here has been developed for Bridgman solidification[21,22] and after for laser pulsed melting[23]. There is good evidence that solidification models apply to solid-state phase transformations under certain carefully chosen circumstances, giving a new insight[14]. For

this, it is necessary that, as a liquid-solid transformation, the solid-state transformation front is highly mobile and the parent phase has a larger solute diffusion coefficient than the product.

One elegant way to represent the complex interface behavior is through the steady-state interface response, IR, i.e. by the interface temperature versus growth rate for a fixed thermal gradient (Figure 1). The temperature and the related concentration of the growing interface are functions of the initial composition of the alloy, C_0, of the interface velocity, V, and the thermal gradient, G. Figure 1a is a schematic representation of the IR for the liquid-solid transformation[21]. The phase diagram to the left of Figure 1a gives the reference temperatures, liquidus and solidus, for the construction of the interface response. Cells and dendrites are expected in the velocity range given by
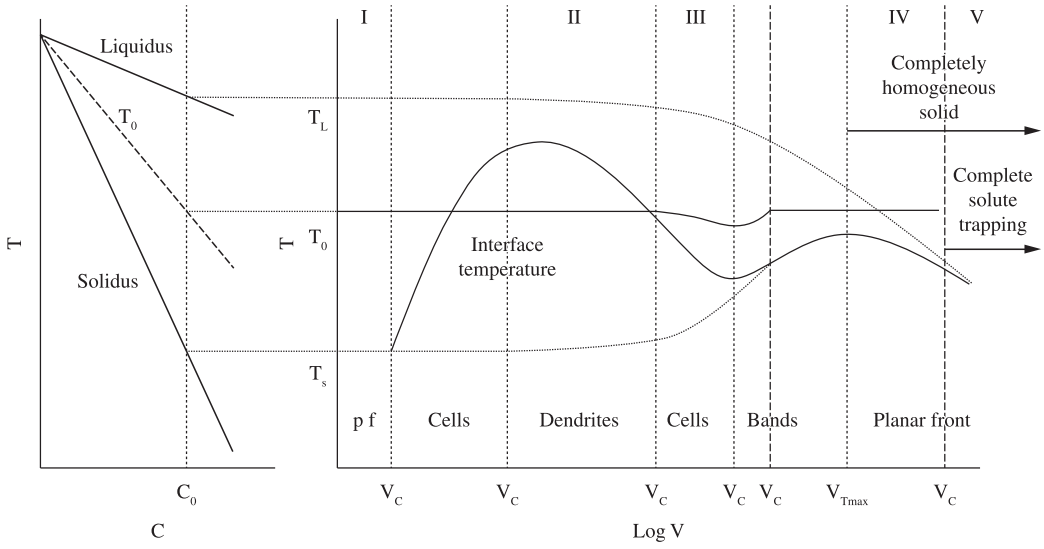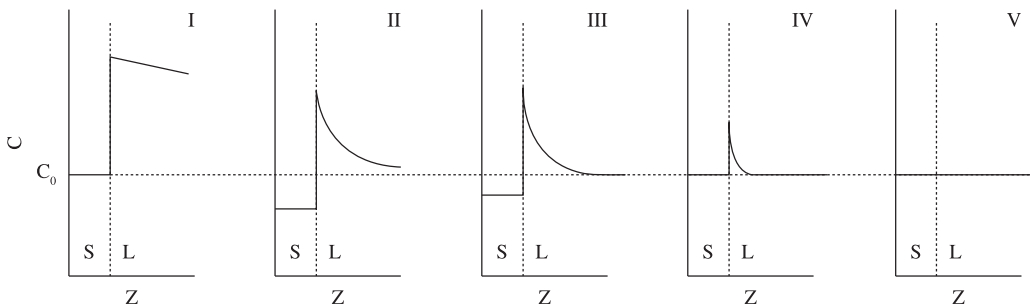
Figure 1. Schematic representation of the microstructural modeling criteria with related IR function (a) and the effect of growth speed on the solute spike (b). Schematic drawings of the interface morphology (c) are also shown.

the limits of constitutional undercooling, Vc, and absolute stability, Va. Plane front growth occurs below Vc and above Va (Figure 1c). Figure 1b shows the evolution of the solute spike near the interface for five representative cases for the hypothetical phase diagram (Figure 1a) with $k_e < 1$. The effect of solute trapping can be seen in the reduction between the solid and liquid compositions at the interface with increasing velocity (Figure 1b), and by the decrease of the liquidus/solidus interval (Figure 1a). Cases "A", "D" and "E" represent steady-state plane front morphologies. Composition invariance is the result of any steady-state plane front growth. Therefore, case "A" corresponds to the local equilibrium, "D" to partial solute trapping, and "E" to complete solute trapping. The boundary layer in the liquid has amplitude C_0/k_v and a characteristic thickness of D/V.

At low velocities a planar interface is stable to perturbations if the thermal gradient is larger than the liquidus-temperature gradient at the interface (Figure 1c). The lower plane front limit is given by the constitutional undercooling criterion[24] (Equation 1):

$$V_C = \frac{\overline{G}D}{\Delta T_0} \tag{1}$$

where the conductivity-weighted temperature gradient is $\overline{G} = (G_S \kappa_S + G_L \kappa_L)/(\kappa_S + \kappa_L)$, with G_i and k_i the temperature gradient and conductivity of phase i (liquid and solid, respectively), D is the solute diffusion coefficient in the parent phase, and $\Delta T_0 (= T_1 - T_s)$ is the equilibrium liquidus-solidus interval. When non-equilibrium conditions prevail at the transformation front, the liquidus is reduced and the solidus raises, both approaching T_0. Further, at high velocities, the transformation temperature decreases due to attachment kinetic undercooling. The liquidus-solidus interval is therefore a function of the interface velocity, $\Delta T_0(V)$. At very low velocities the liquidus-solidus interval is effectively constant while at higher V, when solute trapping begins, it decreases. For a linearized phase diagram (Equation 2):

$$\Delta T_0(V) = T_l(V) - T_s(V) = C_0 m_v \frac{(k_v - 1)}{k_v} \tag{2}$$

where C_o is the alloy composition, m_v is the velocity dependent non-equilibrium liquidus slope and k_v is the non-equilibrium partition coefficient[25]. Equation 2 reduces to ΔT_0 when k_v approaches the equilibrium value k_e.

As presented in the continuous growth model for dilute solutions[26-28,2] the non-equilibrium partition coefficient (k_v) and non-equilibrium liquidus slope (m_v) can be calculated from the equilibrium values k_e and m_e, as (Equations 3 and 4):

$$k_v = \frac{k_e + V/V_d}{1 + V/V_d} \tag{3}$$

$$m_v = m_e \frac{1 - k_v \left[1 - \ln\left(k_v/k_e \right) \right]}{1 - k_e} \tag{4}$$

where V_d is the diffusion velocity across the interface that may be approximated by the ratio of the solute diffusivity across the interface (D_i) to the thickness of that interface (a_0).

In steady state, the plane front grows at the solidus isotherm and the interface compositions in the liquid and solid are $C_1^* = C_0/k_v$ and $C_s^* = C_0$, respectively. This situation corresponds to case A in Figure 1 when $k_v = k_e$. Above V_C the interface adopts a cellular or dendritic morphology, the growth temperature (T*) rises above the solidus and the cell/dendrite tips incorporate less solute than C_o (Figure 1b, "B" and "C"). For cellular/dendritic growth, the tip temperature, T* is given by[21,29] (Equation 5):

$$T^* = T_l + C_l^* (m_v - m_e) - \frac{2\Gamma}{R} - \frac{\overline{G}D}{V} \tag{5}$$

where T_1 is the liquidus temperature for the initial composition of the alloy, Γ is the Gibbs-Thomson coefficient, R is the dendrite tip radius. The dendrite tip radius is calculated as the minimum value of R in the following Equation 6:

$$4\pi^2 \Gamma + 2R \frac{Pe.C_o.m_v.(1 - k_v).\xi_c}{1 - (1 - k_v)Iv(Pe)} + GR^2 = 0 \tag{6}$$

where ξ_c is a stability parameter, and Pe and Iv(Pe) are the Péclet number (=RV/2D) and Ivantsov function of Péclet, respectively[30].

At high velocities, a cellular microstructure is stabilized again and the microstructure becomes finer. When the velocity reaches the upper limit diffusion becomes localized and capillary phenomena dominate so that plane-front growth reappears (case "D" of Figure 1). This occurs beyond the limit of absolute stability, V_a, given by[31,32] (Equation 7):

$$V_a = \frac{\Delta T_0 (V)D}{k_v \Gamma} \tag{7}$$

once plane front growth is stable again, the composition of the solid is C_o and the composition of the liquid depends on the growth velocity. The solution for a planar-front is obtained from the non-equilibrium liquid composition at the interface, C_1^*, which could be calculated using[33] Equation 8.

$$C_l^* = \frac{C_l^e}{1 + \dfrac{k_e - k_v \left(1 - \ln k_v/k_e \right)}{1 - k_e}} \tag{8}$$

where C_1^e is the equilibrium liquidus composition.

Beyond absolute stability, when dT/dV>0, oscillatory instabilities may occur. This phenomenon, known as banding, is produced by the alternate growth of two structures[33,34]. Such oscillatory structures however do not seem to form if the distribution coefficient is close to unity, as is the case of the studied alloy. In the current analyses, the plane-front temperature T_p is calculated from the phase diagram with the necessary non-equilibrium corrections (Equations 3 and 4). Thus (Equation 9):

$$T_p = T_f + m_v C_o / k_v - \Delta T_k \tag{9}$$

where T_f is the melting point of the solvent and ΔT_k is the atom attachment undercooling. With increasing V, the non-equilibrium solidus temperature rises close to T_0 when solute trapping becomes important (effect of second term on the RHS of Equation 9). At even higher velocities, attachment kinetics becomes the dominant mechanism (third term on the RHS of Equation 9) and the plane front temperature decreases (D and E in Figure 1a).

For collision-limited growth of a rough interface, the value of the atom attachment undercooling is, to a first approximation[35] (Equation 10):

$$\Delta T_k = \frac{R_g T_f}{V_0 \Delta S_t} V \tag{10}$$

where R_g is the gas constant, V_0 is the sound speed in the solid and ΔS_t is the molar entropy of transformation.

Up to now one considers a binary system but in most engineering cases, like the present one, the system is multicomponent. Gilgien and others[19,22] extended the analyses for the multicomponent case, which can be valid as long as every solute diffuses independently. For a multicomponent alloy, the limit of constitutional undercooling is a sum of i-components. Considering a linearized phase diagram, Equation 1 is then[36,37] (Equation 11):

$$V_C = \bar{G} \sum_i \frac{k_i D_i}{m_i C_{0,i}(k_i - 1)} \tag{11}$$

For a multicomponent alloy, Equations 3 and 4 must be applied for each component and the parameters become $k_{v,i}$, $k_{e,i}$ and $V_{d,i}$. As in the case of V_c, the absolute stability limit must be considered as a sum over i-solutes, giving (Equation 12):

$$V_a = \sum_i \frac{m_{v,i} C_{0,i}(k_{v,i} - 1) D_i}{k_{v,i}^2 \Gamma} \tag{12}$$

The out-of-equilibrium liquidus slope, $m_{v,i}$, is given by (Equation 13):

$$m_{v,i} = \frac{1 - k_{v,i}\left[1 - \ln\left(k_{v,i}/k_{e,i}\right)\right]}{1 - k_{e,i}} m_{e,i} \tag{13}$$

The phase growth temperature during cellular and dendritic growth is the liquidus minus a undercooling. When the growth speed is below the diffusive speed ($V \ll V_d$), the interface undercooling is composed by the curvature undercooling and the solute rejection undercooling. For a multicomponent alloy, the dendrite tip temperature is (Equation 14):

$$T^* = T_l + \sum_i C_{l,i}^*\left(m_{v,i} - m_{e,i}\right) - \frac{2\Gamma}{R} - \frac{\bar{G}D}{V} - \Delta T_k \tag{14}$$

Where T_l is the liquidus temperature of the alloy at the initial composition, C_l^* is the liquid composition in contact with the dendrite tip, Γ is the Gibbs-Thomson coefficient, R is the dendrite tip radius and ΔT_k is the atomic attachment undercooling.

3. Experimental

Swiss Steels Ltd. supplied the AISI 410S alloy in the form of a 10 mm diameter rolled bar. The analyzed composition is presented in Table 1 and the correspondingly phase diagram as calculated by the SSOL Thermocalc database[38] is shown in Figure 2. This phase diagram corresponds to a Fe-Cr section for the multicomponent alloy with initial Cr-composition indicated by the dashed line. Table 2 presents additional physical-chemistry data from references 38 to 42.

The interface thickness was considered as 2 nm for the solid/liquid interface[29], and equal to the lattice parameter of the ferrite (2.8 Å) for the ferrite/austenite transformation. The diffusivity of others elements than Cr in iron were obtained in the references 39 and 7 for both liquid and ferrite phases.

The isovelocity experiments were carried out in a Bridgman furnace with a liquid metal cooling system (Ga-In-Sn alloy) for efficient quenching. Each sample was melted in a 6 mm I.D. alumina tube inserted in a radiation vertical furnace and lowered into the liquid metal bath at rapid rate (33 μm/s). When the alumina tube with the specimen penetrated about 8 cm into the cooling bath, the speed was reduced to the selected value. This ensured a steady state temperature profile in the specimen. In the present study the selected velocities were 5, 10 and 100 μm/s. At a given moment, the tube was dropped into the liquid, thus producing a snapshot of the growth microstructures at high temperatures. An experiment using an alumina-encapsulated thermocouple inserted in the axis of the bar was used to evaluate the thermal profile, and

Table 1. Chemical composition, in wt. (%), of the AISI 410S sample (Fe balance).

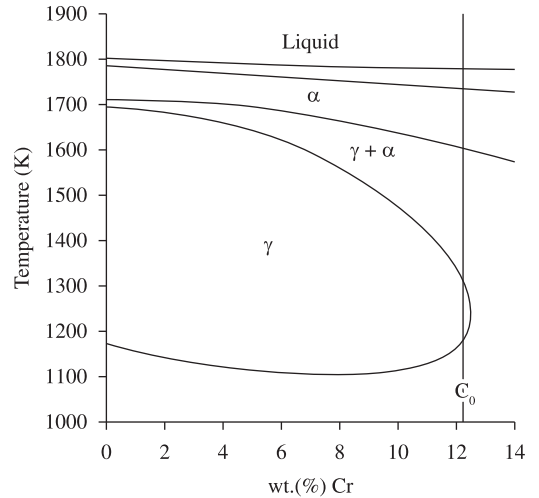| C	Si	Mn	P	S	Ni	Cr	Cu	Mo	V
0.02	0.91	0.39	0.025	0.007	0.45	12.27	0.08	0.03	0.06

Figure 2. Pseudo-binary phase diagram of the AISI 410S alloy in a Fe-Cr section. The initial composition (C_0) is shown.

Table 2. Physical properties of the alloy for both transformations.

	Solidification	Ferrite/austenite
Liquidus (K)	1774.11	1587.74
Solidus (K)	1729.26	1283.60
D_{Cr}(solidus) (m²/s)	3×10^{-9}	4.27×10^{-14}
Γ (m.K^{-1})	1.9×10^{-7}	5.5×10^{-6}
ΔH (J.mol^{-1})	11'300	8'370
ΔS (J.mol^{-1}.K)	6.4	6.5
V_0 (m/s)	2000	5000

thus used to predict phase transformation temperatures and thermal gradient. The thermocouple experiment was carried out at 10 μm/s.

A CW-CO$_2$ laser was focused to a 0.5 mm spot diameter on the steel surface. The temperature history at centerline was evaluated using Rosenthal method[44]. The macroscopic shape of melt pool was used to calibrate the laser-steel absorption.

Microstructural analyses were carried out using optical microscopy. The samples were cut and polished using standard techniques, and subsequently electrolytically etched in an aqueous solution of CuCl$_3$.

4. Results

4.1. *Bridgman growth*

Directional growth experiments produced ferrite single-crystals with different interface microstructures in different growth speeds, Figure 3: a planar interface at 5 μm/s, a cellular interface at 10 μm/s, and a dendritic interface at 100 μm/s.

The average thermal gradients were evaluated using the thermocouple experiment, giving: 18 K.mm^{-1} for solidification and 40 K.mm^{-1} for ferrite-austenite transformation.

The average spacing between cells or dendrites was 144 ± 8 and 95 ± 14 μm, for the samples grown at 10 and 100 μm/s respectively. Using this data and Equation 6, the cell/dendrite tip radii were evaluated as 5.9 and 2.6 μm, respectively. The solidification interfaces were concave as result of heat and solute convection in the liquid (Figure 3a). Additionally, for the 5 μm/s sample, the crystal presented lateral facets indicating that the crystal grown in the <001> direction. The measured solidification temperatures for the three growth speeds were situated at 1730 ± 20 K for the planar interface, and at 1750 ± 20 K for the other two conditions. The errors are due to uncertainties on the position of the interfaces.

The first austenite precipitates were dendritic and plate-like for the growth speeds of 5 and 10 μm/s as can be seen in Figure 4a. In the case of 100 μm/s, the early austenite was always plate-like. For all growth speeds the growth temperatures were situated around 1300 K. Table 3 summarizes the observations of morphology and temperatures for the directional growth samples.

Grains, formed in lower temperatures, were partially transformed to martensite during quenching, Figure 4b. Metallographic analyses shown that the austenite precipitates have not a preferential growth direction in respect to the ferrite matrix.
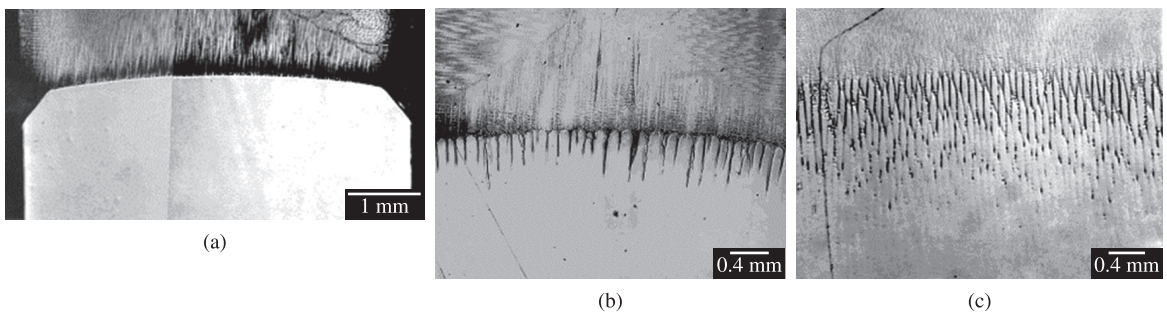

(a)

(b)

(c)

Figure 3. Bridgman samples cross-section near solid-liquid interphase. a) 5 μm/s, b) 10 μm/s, and c) 100 μm/s. Growth direction is upwards.
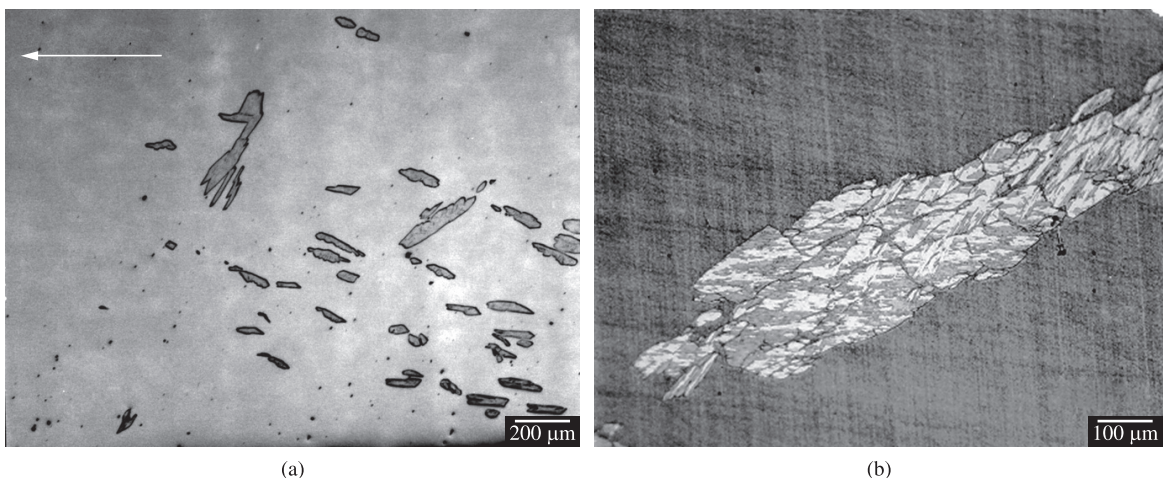

(a)

(b)

Figure 4. a) Precipitates of austenite in the ferrite matrix, Bridgman, 5 μm/s. The arrow indicates the growth direction; b) Austenite grains partially transformed in martensite (dark phase) after quenching.

Table 3. Summary of directional growth experiments results.

V (µm/s)	Solidification			Solid-state transformation	
	Morphology	λ (µm)	T_{sol} (K)	Morphology	T_{ss} (K)
5	Planar	-	1730 ± 20	Dendritic	1250 ± 20
10	Cellular	144	1750 ± 20	Dendritic	1330 ± 20
100	Dendritic	95	1750 ± 20	Dendritic	1310 ± 20

4.2. *Laser remelting*

The solidification microstructure of laser-remelted samples was dendritic forming grains, Figure 5. The grains grown to the centerline and became finer as laser scanning speed was increased. Differently of Bridgman experiments, it was not possible to measure the temperature of the dendritic front for laser remelting.

In scanning speeds between 0.3 and 10 mm/s, it was possible to observe austenite precipitates in the remelted trace. These precipitates can cross grain boundaries and were plate-like, Figures 6a and b. As can be seen, the austenite precipitates can nucleate inter- or intra-granular depending on the grain boundary density of the laser track. Laser experiments from 0.3 to 0.6 mm/s produced precipitates at the same order of temperatures of Bridgman experiments, i.e. around 1000 °C, Figure 7. Above this velocity the temperature drops to reach 900 °C at 10 mm/s. Above 10 mm/s, the precipitates disappeared from the remelted trace.

4.3. *Calculations*

Solidification under Bridgman: V_c and V_a were calculated giving 1.34 µm/s and 0.75 m/s, respectively. For the 5 µm/s experiment the planar interface is at solidus. For the 10 and 100 µm/s experiments the temperatures can be evaluated by the measured average tip radii together with Equation 7. The results are presented in Table 4.

Ferrite-austenite transformation: The interface response for the ferrite-austenite is presented in Figure 7 together with the experimental results. V_c and V_a were calculated giving 5.7×10^{-12} m/s and 13.3 µm/s, respectively. Therefore, for the current steel, composition invariant transformation of ferrite into austenite (planar front) was expected above 13.3 µm/s.

5. Discussion

Since the temperature near to the tube wall is higher than in the center of the tube, the liquid at periphery rises up and the liquid near the axis of the tube moves downwards. This convection will lead to a lateral rejection of solute and to a curved solid/liquid interface, Figure 3a. In addition, this convection disrupts the solute built-up in the front of the growing interface leading to a stabilization of the interface[13]. This stabilization effect is reflected by an extension of planar growth range during solidification; the calculated constitutional undercooling velocity, $V_c = 1.34$ µm/s, is below that evaluated by Bridgman experiments 5 µm/s < V_c < 10 µm/s.

The temperature measurements were not very precise but some general tendencies can be verified. The measured solidification temperature for planar front, V = 5 µm/s,
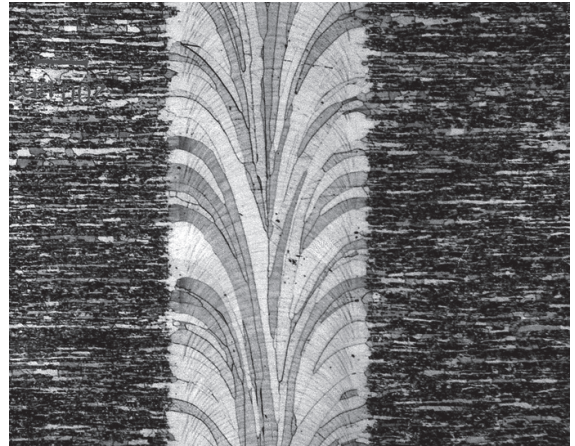

Figure 5. Upper view of a laser remelting trace at 5 mm/s. Laser displacement downwards.

was in good agreement with solidus; the measured value of solidification temperature being about 1730 K for a calculated solidus of 1729.26 K. On the other hand, the other two growth temperatures, for V = 10 and 100 µm/s, presented fairly agreement between calculations and experiments. The measured growth temperatures rest at about 1750 K for both 10 and 100 µm/s experiments, when calculated results predict 1769 and 1773 K, respectively. This could be also linked to the errors in determining precisely the interface position since some differences could occur in the temperature history, albeit the three directional growth experiments were performed in similar conditions.

Some of the early austenite precipitates during the Bridgman experiments (5 and 10 µm/s) presented dendritic morphology, Figure 4. Chromium segregation was observed near these dendrites[45], as expected for a composition variant transformation. On the other hand, plate-like precipitates (above 100 µm/s) had the same composition of the surrounding ferrite. These results are in good agreement with theoretical predictions for composition variant/invariant austenite growth, as the calculated value of V_a for ferrite-austenite transformation was 13.3 µm/s. This fact, the absence of orientation relationship with the matrix and the characteristic of crossing grain boundaries, shown that massive austenite is obtained above V_a.

The austenite start temperature, as determined in the directional growth and the laser experiments were near to inferior solvus for growth speeds up to 0.6 mm/s; after this velocity the temperature drops, Figure 7. Taking the Continuous Growth Model (CGM) into account, it was expected a temperature increase due to solute trapping effect,
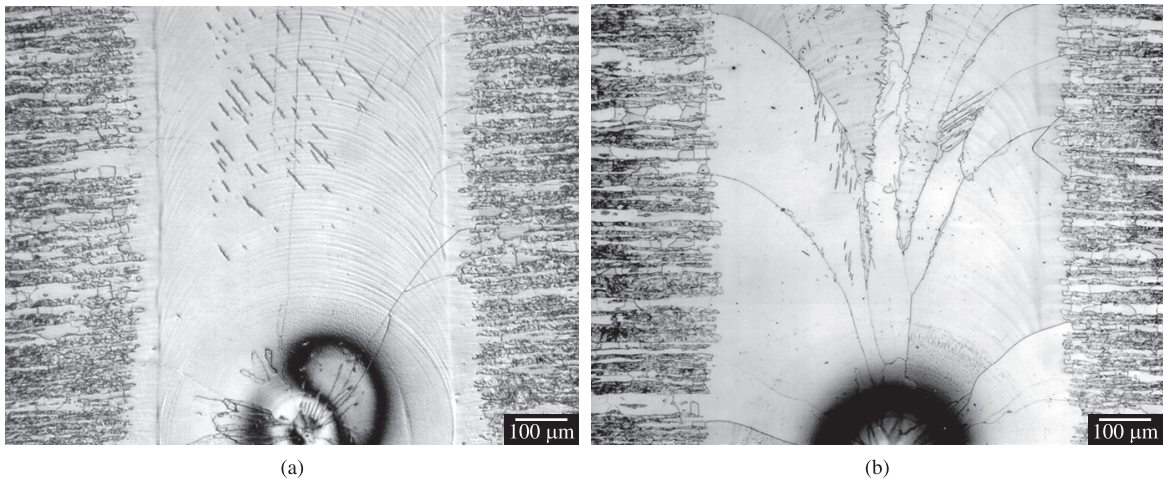
(a)　　　　　　　　　　　　　　　　　　　　　　　　　　(b)

Figure 6. Laser remelted traces near to the final liquid bath position (quenching). a) 0.4 mm/s and b) 0.6 mm/s. Laser displacement downwards.
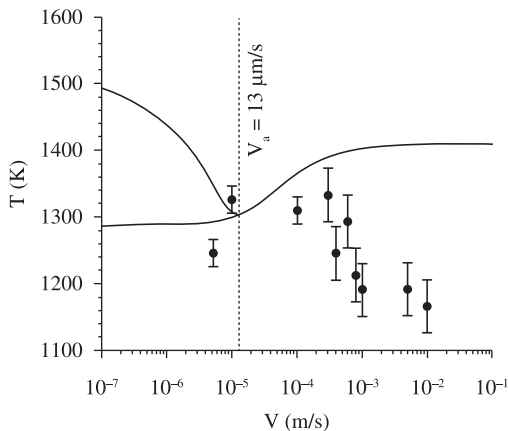

Figure 7. Growth temperatures of austenite in ferrite. Experimental measurements are circles and the calculated interface functions are lines.

Table 4. Calculated values of austenite phase growth during directional solidification.

V (μm/s)	T (K)
5	1729.26
10	1768.65
100	1773.44

which was not actually verified. These results led to believe that the atomic attachment undercooling (Equation 10) took place earlier than expected by the model. This could be understood as a consequence of an interface that is not completely rough, but contain a given number of steps to fix the atoms of the parent phase. Therefore, not all sites at the interface are low-energy sites and some atoms must migrate in the parent phase to find an adequate position. This assumption is also valid for the growth of austenite across grain boundaries, Figure 6. The incoherent side of the precipitates grown faster than the coherent one, since more

coherent is the interphase boundaries less low-energy sites are available in the parent phase. It seems that this relationship between incoherency and the austenite growth was also verified during directional growth, since the precipitates growth was not aligned to the solidification growth direction.

A limiting velocity exists for both solidification conditions and solid-state transformations. For the ferrite-austenite reaction, the limiting growth velocity is given by the retained ferrite limit. Once the atoms, attached to the ferrite structure, have not sufficient time to jump into the austenite crystal, the primary phase is retained. The limiting velocity was at 10 mm/s for the present alloy, as determined in laser experiments.

The AISI 410S alloy is essentially a ferritic alloy, which can eventually develop a duplex structure when correctly treated. It seems that 1000 °C is the correct temperature to generate austenite during continuous cooling. However, the temperature drops due to the atomic attachment and the undercooling must to be taking in account for growth speeds between 0.6 and 10 mm/s. In terms of corrosion, better results can be obtained when the austenite phase can be generated without segregation. If austenite precipitates grow massively the chromium composition will be homogenous everywhere, thus sensitization is avoided. Massive austenite is obtained above V_a, i.e. above 13 μm/s, and below the retained ferrite limit, 10 mm/s.

6. Conclusions

The microstructure formation of AISI 410S stainless steel and phase growth modeling were investigated using directional growth and laser melting techniques.

• Thermal and solute convection ahead the solidification interface during the directional solidification led to an additional stabilization of the planar growth mode. The limit of constitutional undercooling was observed as growth rates between 5 and 10 μm/s, for a theoretical value of 1.34 μm/s. The solidification temperature was measured as 1730 K for the growth rate of 5 μm/s experiment, and 1750 K for 10 and 100 μm/s growth rates;

- Directional growth experiments (5-10 µm/s) produced plate-like and dendritic austenite precipitates in the solid-state. The 100 µm/s directional growth and the laser experiments (0.3-10 mm/s) produced plate-like austenite. The appearance of dendrites, with the consequent segregation of the elements, can be prior expected by the current microstructure modeling;
- The ferrite/austenite boundary is not completed rough, as described in the continuous growth model for solidification, since the interface temperature decreased with increased growth speed, Figure 7. At atomic level, not all the interface present low-energy sites for the incoming ferrite atoms, increasing the necessary undercooling for the transformation;

- Massive austenite can be produced at growth rates from 0.3 to 10 mm/s, and temperatures between 1100 and 1300 K. Since this phase is produced without microsegregation, the structure is less sensitive to corrosion. Above growth velocity of 10 mm/s, the austenite is not formed anymore, and retained ferrite is verified.

Acknowledgements

References

1. Pohl M, Reich W, Ibach A and Wischnewski F. Schweizer Maschinenmarkt. *Swiss Association for Materials Science and Technology SVMT*. 1998; (5).

2. Harvey PD, editor. *Engineering Properties of Steels*. Metals Park: American Society for Metals; 1982. 527 p.

3. Boyer HE and Gall TL, editors. *Metals Handbook*. 10th ed. Materials Park: American Society for Metals; 1990. 2521 p. v. 1: Properties and Selection: Irons, Steels, and High-Performance Alloys.

4. Krishna BV and Bandyopadhyay, A. Surface modification of AISI 410 stainless steel using laser engineered net shaping, *Materials and Design.* 2009; 30:1490-1496. http://dx.doi.org/10.1016/j.matdes.2008.08.003

5. Koch GH, Brongers MPH, Thompson NG, Virmani YP and Payer, JH. *Corrosion Cost and Preventive Strategies in the United States*. McLean: Office of Infrastructure Research and Development; 2001. 773 p. Technical report FHWA-RD-01-156.

6. Paredes RSC, Borsato KS, Bernardini PAN and Aguila JV. Avaliação da soldabilidade de aços inoxidáveis especiais a ser utilizados na indústria do petróleo. In: *Anais do II Congresso Brasileiro de P&D em Petróleo & Gás*; 2003; Rio de Janeiro. Rio de Janeiro; 2003.

7. Machado JPSE, De Abreu HFG, Sobral AVC and De Sant´Ana HB. Influência do óleo nacional pesado na corrosão dos aços inoxidáveis. In: *Anais do II Congresso Brasileiro de P&D em Petróleo & Gás*; 2003; Rio de Janeiro. Rio de Janeiro; 2003.

8. McCrink EJ. *Seam-welded air hardenable steel constructions*. Patent US 10519910. 2004. Avaliable from: <http://patft.uspto.gov/>. Access in: 28/07/2010.

9. Reick W, Pohl M and Padilha AF. O desenvolvimento dos aços inoxidáveis ferríticos-austeníticos com microestrutura duplex - histórico e perspectivas futuras. In: *Anais do 47º Congresso Anual da ABM*; 1992; Belo Horizonte. Belo Horizonte; 1992. v. 1; p. 557-574.

10. Shek CH, Dong C, Lai JKL and Wong KW. Early-Stage Widmanstätten Growth of the Phase in a Duplex Steel. *Metallurgical and Materials Transactions A*. 2000; 31A:15-19.

11. Aminorroaya S, Reid M and Dippenaar R. Simulation of microsegregation and the solid/liquid interface progression in the concentric solidification technique. *Modelling and Simulation in Materials Science and Engineering.* 2011; 19:025003. http://dx.doi.org/10.1088/0965-0393/19/2/025003

12. Hurle DTJ, editor. *Bulk crystal growth - Basic techniques*. Handbook of crystal growth. Amsterdam: Elsevier; 1994. 658 p. v. 2.

13. Trivedi R, Miyahara H, Mazumder P, Simsek E and Tewari SN. Directional Solidification Microstructures in Diffusive and Convective Regimes. *Journal of Crystal Growth.* 2001; 222:365-379. http://dx.doi.org/10.1016/S0022-0248(00)00761-2

14. Lima M and Kurz W. Massive Transformation and Absolute Stability. *Metallurgical and Materials Transactions*. 2002; 33A:2337-2345. http://dx.doi.org/10.1007/s11661-002-0357-1

15. Jacot A, Sumida M and Kurz W. Solute trapping-free massive transformation at absolute stability. *Acta Materialia.* 2011; 59:1716-1724. http://dx.doi.org/10.1016/j.actamat.2010.11.038

16. Gremaud M, Allen DR, Rappaz M and Perepezko JH. The development of nucleation controlled microstructures during laser treatment of Al-Si alloys. *Acta Materialia*. 1996; 44:2669-2681. http://dx.doi.org/10.1016/1359-6454(95)00393-2

17. Gill SC and Kurz W. Rapidly solidified Al-Cu alloys: II. Calculation of the microstructure selection map. *Acta Metallurgica et Materialia*. 1995; 43:139-151.

18. Lippautz S, Zimmermann M, Kurz W and Jeglitsch J. *Sonderbände der Praktischen Metallographie*. 1991; 22:409-412.

19. Lima MSF, Gilgien P and Kurz W. Microstructure Selection in Laser Remelted Fe-C-Si Alloys. *Zeitschrift für Metallkunde*. 1998; 89:751-757.

20. Fukumoto S and Kurz W. Solidification phase and microstructure selection maps for Fe-Cr-Ni alloys. *ISIJ International*. 1998; 38:71-77. http://dx.doi.org/10.2355/isijinternational.38.71

21. Trivedi R and Kurz W. Dendritic growth. *International Materials Reviews*. 1994; 39:49-74.

22. Gilgien P and Kurz W. Microstructure selection in binary and ternary alloys. *Materials Science and Engineering*. 1994; A178:199-201.

23. Smith PM and Aziz MJ. Solute trapping in aluminum alloys. *Acta Metallurgica et Materialia*. 1994; 42:3515-3525. http://dx.doi.org/10.1016/0956-7151(94)90483-9

24. Tiller WA, Jackson KA, Rutter JW and Chalmers B. The redistribution of solute atoms during the solidification of metals. *Acta Metallurgica*. 1953; 1:428-437. http://dx.doi.org/10.1016/0001-6160(53)90126-6

25. Boettinger WJ and Coriell SR. *Science and Technology of the Undercooled Melt*. Dordrecht; 1986. p. 81. NATO ASI Series 114.

26. Aziz MJ. Model for solute redistribution during rapid solidification. *Journal of Applied Physics*. 1982; 53:1158-1169. http://dx.doi.org/10.1063/1.329867

27. Aziz MJ and Kaplan T. Continuous growth model for interface motion during alloy solidification. *Acta Metallurgica*. 1988; 36 :2335-2347. http://dx.doi.org/10.1016/0001-6160(88)90333-1

28. Aziz MJ. Interface attachment kinetics in alloy solidification. *Metallurgical & Materials Transactions A*. 1996; 27A:671-686. http://dx.doi.org/10.1016/0001-6160(86)90056-8

29. Kurz W, Giovanola B and Trivedi R. Theory of microstructural development during rapid solidification. *Acta Metallurgica et Materialia*. 1986; 34:823-830. http://dx.doi.org/10.1016/0001-6160(86)90056-8

30. Kurz W and Fisher DJ. *Fundamentals of Solidification*. 4th ed. Switzerland: Trans Tech Publications; 1998. 247 p.

31. Mullins WW and Sekerka RF. The Stability of a Planar Interface During Solidification of a Dilute Binary Alloy. *Journal of Applied Physics*. 1989; 35:444-451. http://dx.doi.org/10.1063/1.1713333

32. Huntley DA and Davis SH. Thermal effects in rapid directional solidification: linear theory. *Acta Metall. Mater.* 1993; 41:2025-2043. http://dx.doi.org/10.1016/0956-7151(93)90373-Z

33. Carrard M, Gremaud M, Zimmermann M and Kurz W. About the banded structure in rapidly solidified dendritic and eutectic alloys. *Acta Metallurgica et Materialia*. 1992; 40:983-996. http://dx.doi.org/10.1016/0956-7151(92)90076-Q

34. Kurz W and Trivedi R. Banded solidification microstructures. *Metallurgical & Materials Transactions*. 1996; 27A:625-634. http://dx.doi.org/10.1007/BF02648951

35. Turnbull D. On the relation between crystallization rate and liquid structure. *Journal of Physical Chemistry*. 1962; 66:609-613. http://dx.doi.org/10.1021/j100810a009

36. Coriell SR, McFadden GB, Voorhees PW and Sekerka RF. Stability of a Planar Interface During Solidification of a Multicomponent System. *Journal of Crystal Growth*. 1987; 82:295-302. http://dx.doi.org/10.1016/0022-0248(87)90317-4

37. Hunziker O. Theory of plane front and dendritic growth in multicomponent alloys. *Acta Materialia*. 2001; 49:4191-4203. http://dx.doi.org/10.1016/S1359-6454(01)00313-5

38. ThermoCalc thermodynamic database. version J. Sweden: Stockholm Royal Institute; 1994.

39. Iida T and Guthrie RIL. *The Physical Properties of Liquid Metals*. Oxford: Claredon Press; 1987. 223 p.

40. Koseki T, Matsumiya T, Yamada W and Ogawa T. Numerical modeling of solidification and subsequent transformation of Fe-Cr-Ni alloys. *Metallurgical & Materials Transactions A*. 1994; 25A:1309-1321.

41. Porter DA and Easterling KE. *Phase Transformations in Metals and Alloys*. 2th ed. London: Chapman & Hall; 1992. 514 p.

42. Lide DR, editor. *Handbook of Chemistry and Physics*. 78th ed. Florida: CRC Press; 1997. p. 14-36.

43. Brandes EA, editor. *Smithels Metals Reference Book*. 6th ed. London: Butterworths; 1986.

44. Rosenthal D. The theory of moving sources of heat and its application to metal treatments. *Trans A.S.M.E.* 1946; 849-866.

45. Lima MSF, Heinemann WA and Kurz W. *Final Report Korrosionsbeständiger Bewehrungsstahl*. Institut für Baustoffe, Werkstoffchemie und Korrosion; 1998. 7 p.